

Photometric and spectroscopic study of the burst-like brightening of two *Gaia*-alerted young stellar objects

Zsófia Nagy,^{1,2}★ Péter Ábrahám,^{1,2,3} Ágnes Kóspál,^{1,2,3,4} Sunkyung Park,^{1,2} Michał Siwak,^{1,2} Fernando Cruz-Sáenz de Miera,^{1,2} Eleonora Fiorellino,^{1,2,5} David García-Álvarez,^{6,7} Zsófia Marianna Szabó,^{1,2,8,9} Simone Antonucci,⁵ Teresa Giannini,⁵ Alessio Giunta,¹⁰ Levente Kriskovics,^{1,2} Mária Kun,^{1,2} Gábor Marton,^{1,2} Attila Moór,^{1,2} Brunella Nisini,⁵ Andras Pál,^{1,2,3} László Szabados,^{1,2} Paweł Zieliński,¹¹ Łukasz Wyrzykowski¹²

¹Konkoly Observatory, Research Centre for Astronomy and Earth Sciences, Eötvös Loránd Research Network (ELKH),

H-1121 Budapest, Konkoly Thege Miklós út 15-17., Hungary

²CSFK, MTA Centre of Excellence, Budapest, Konkoly Thege Miklós út 15-17., H-1121, Hungary

³ELTE Eötvös Loránd University, Institute of Physics, Pázmány Péter sétány 1/A, H-1117 Budapest, Hungary

⁴Max Planck Institute for Astronomy, Königstuhl 17, D-69117 Heidelberg, Germany

⁵INAF-Osservatorio Astronomico di Roma, via di Frascati 33, 00078, Monte Porzio Catone, Italy

⁶Instituto de Astrofísica de Canarias, Avenida Vía Láctea, E-38205 La Laguna, Tenerife, Spain

⁷Grantecan S.A., Centro de Astrofísica de La Palma, Cuesta de San José, E-38712 Breña Baja, La Palma, Spain

⁸Max-Planck-Institut für Radioastronomie, Auf dem Hügel 69, 53121 Bonn, Germany

⁹Scottish Universities Physics Alliance (SUPA), School of Physics and Astronomy, University of St Andrews, North Haugh, St Andrews, KY16 9SS, UK

¹⁰Space Science Data Center, Italian Space Agency, via del Politecnico, 00133, Roma, Italy

¹¹Institute of Astronomy, Faculty of Physics, Astronomy and Informatics, Nicolaus Copernicus University in Toruń,

ul. Grudziądzka 5, 87-100 Toruń, Poland

¹²Astronomical Observatory, University of Warsaw, Al. Ujazdowskie 4, 00-478, Warsaw, Poland

Accepted XXX. Received YYY; in original form ZZZ

ABSTRACT

Young stars show variability on different time-scales from hours to decades, with a range of amplitudes. We studied two young stars, which triggered the *Gaia* Science Alerts system due to brightenings on a time-scale of a year. *Gaia*20bwa brightened by about half a magnitude, whereas *Gaia*20fgx brightened by about two and half magnitudes. We analyzed the *Gaia* light curves, additional photometry, and spectra taken with the Telescopio Nazionale Galileo and the Gran Telescopio Canarias. Several emission lines were detected toward *Gaia*20bwa, including hydrogen lines from H α to H δ , Pa β , Br γ , and lines of Ca II, O I, and Na I. The H α and Br γ lines were detected toward *Gaia*20fgx in emission in its bright state, with additional CO lines in absorption, and the Pa β line with an inverse P Cygni profile during its fading. Based on the Br γ lines the accretion rate was $(2.4 - 3.1) \times 10^{-8} M_{\odot} \text{ yr}^{-1}$ for *Gaia*20bwa and $(4.5 - 6.6) \times 10^{-8} M_{\odot} \text{ yr}^{-1}$ for *Gaia*20fgx during their bright state. The accretion rate of *Gaia*20fgx dropped by almost a factor of 10 on a time-scale of half a year. The accretion parameters of both stars were found to be similar to those of classical T Tauri stars, lower than those of young eruptive stars. However, the amplitude and time-scale of these brightenings place these stars to a region of the parameter space, which is rarely populated by young stars. This suggests a new class of young stars, which produce outbursts on a time-scale similar to young eruptive stars, but with smaller amplitudes.

Key words: Stars: variables: T Tauri – stars: pre-main sequence

1 INTRODUCTION

About half of young stellar objects (YSOs) show photometric variations on daily-weekly timescales, with typical values of a few times 0.1 mag at optical and infrared wavelengths (e.g. [Megath et al. 2012](#)). Some young stars show brightness variations on even longer time-scales: months, years, centuries. These variations are related to different physical processes ([Hillenbrand & Findeisen 2015](#)). Some

of the light variations are periodic, and are related to photospheric inhomogeneities, such as starspots. Periodic or quasi-periodic dips in the light curves can be related to circumstellar dust passing through the line of sight toward the star. One example of this phenomenon is the class of AA Tau-type stars, where the occultations are caused by an inner disk warp (e.g. [Bouvier et al. 1999, 2003, Cox et al. 2013, Nagy et al. 2021](#)). Aperiodic events can also occur due to the unsteady mass transfer from the inner disk to the star ([Blinova et al. 2016](#)), including “clumpy accretion” ([Gullbring et al. 1996; Siwak et al. 2018](#)). The eruptive class of young stars shows bright-

★ E-mail: nagy.zsolia@csfk.org

ness variations with an amplitude of a few magnitudes and remain bright on longer timescales. These events are typically called outbursts and are caused by a sudden increase of the mass accretion rate from $10^{-10} - 10^{-8}$ in quiescence up to $10^{-6} - 10^{-4} M_{\odot} \text{ yr}^{-1}$ during outburst. Eruptive young stars are commonly divided into two main classes: EX Lupi-type stars (EXors) and FU Orionis-type stars (FUors). The former show brightenings of 2–4 mag, last for less than a year and are recurrent (e.g. [Herbig 2008](#)); the latter brighten by up to 5 magnitudes and last for several decades (e.g. [Audard et al. 2014](#)). So far the number of confirmed FUors is limited to no more than a dozen while the number of known EXors is limited to less than 25, including candidates ([Audard et al. 2014](#)). Recent studies have shown, that not all the eruptive young stars belong to these two main classes ([Hillenbrand et al. 2019](#), [Hodapp et al. 2020](#)).

ESA’s *Gaia* space telescope has been monitoring the whole sky, determining the parallax and proper motion of 1.8 billion stars. The sources which show significant brightness changes are reported as *Gaia* Photometric Science Alerts ([Hodgkin et al. 2021](#)), which are well suited to identify brightening or fading events of young stars. Two *Gaia* Science alert sources have already been identified and confirmed as FUors: Gaia17bpi ([Hillenbrand et al. 2018](#)) and Gaia18dvy ([Szegedi-Elek et al. 2020](#)), two other *Gaia* alert sources as EXors: Gaia18dvz ([Hodapp et al. 2019](#)) and Gaia20eae ([Cruz-Sáenz de Miera et al. 2022](#)), while two more sources were found to be young eruptive stars other than FUors or EXors: Gaia19ajj ([Hillenbrand et al. 2019](#)) and Gaia19bey ([Hodapp et al. 2020](#)). Another young star, V555 Ori was also reported as a *Gaia* alert due to a brightening event, but was later found to be a result of changing circumstellar extinction rather than an accretion burst ([Nagy et al. 2021](#)). *Gaia* Science alerts were also published for the two targets analyzed below as well.

Gaia20bwa, or 05351885-0444100 in the Two Micron All Sky Survey (2MASS) All-Sky Catalog of Point Sources ([Cutri et al. 2003](#)) ($\alpha_{J2000} = 05^{\text{h}} 35^{\text{m}} 18^{\text{s}}.86$, $\delta_{J2000} = -4^{\circ} 44' 10''.21$), is located in the Orion A star-forming region at 410^{+12}_{-11} pc ([Bailer-Jones et al. 2021](#)). [Tobin et al. \(2009\)](#) found it to be a classical T Tauri star (CTTS), but didn’t rule out the possibility of being a weak-line T Tauri star. [Da Rio et al. \(2016\)](#) determined the effective temperature of Gaia20bwa to be 3142.5 ± 16.0 K and its mass to be $0.206 \pm 0.008 M_{\odot}$. Its brightening by 0.3 mag was reported as a *Gaia* alert on 2020 April 18. Gaia20bwa is part of the catalogue of [Marton et al. \(2019\)](#) with an 85% probability of being a YSO. Gaia20fgx ($\alpha_{J2000} = 22^{\text{h}} 54^{\text{m}} 59^{\text{s}}.09$, $\delta_{J2000} = +62^{\circ} 34' 34''.75$) is located in the Cepheus OB3 association, at about $1.01^{+1.88}_{-0.32}$ kpc ([Bailer-Jones et al. 2021](#)). It had a *Gaia* alert on 2020 November 17 due to a 2.5 mag brightening over a year. Gaia20fgx is also part of the catalogue of [Marton et al. \(2019\)](#) with a 96% probability of being a YSO. [Allen et al. \(2012\)](#) identified this target as a Class II source.

In this paper, we analyze follow-up photometry and spectroscopy of the sources in order to investigate whether their brightening is related to eruptive events or scaled-up version of the normal magnetospheric accretion. In Section 2 we describe the photometric and spectroscopic observations of the sources, in Sect. 3 we explain the results on the light curves, color variations, spectroscopy, spectral energy distributions (SEDs), and accretion rates of the targets. We compare the results to those toward eruptive young stars and CTTS in Sect. 4.

2 OBSERVATIONS

2.1 Photometry

We obtained ground-based optical photometric observations of Gaia20bwa and Gaia20fgx with the 80 cm Ritchey-Chrétien telescope (RC80) at the Piszkestető Mountain Station of Konkoly Observatory (Hungary) and with the 60 cm Carl-Zeiss telescope at Mount Suhora Observatory of the Cracow Pedagogical University (Poland). The RC80 telescope was equipped with an FLI PL230 CCD camera, $0''.55$ pixel scale, $18'.8 \times 18'.8$ field of view, Johnson *BV* and Sloan *g'r'i'* filters. The telescope at Mount Suhora was equipped with an Apogee Aspen-47 camera, $1''.116$ pixel scale, $19'.0 \times 19'.0$ field of view, Sloan *g'r'i'* filters. [Figure 1](#) shows portions of the images taken of our targets. We typically obtained 3 to 13 images in each filter. We first applied CCD reduction including bias, flatfield, and dark current corrections. Then we calculated aperture photometry for the science target and several comparison stars in the field of view using an aperture radius of $2''.75$. We selected those comparison stars from the APASS9 catalog ([Henden et al. 2015](#)) that were within $6'.5$ of the target and which were mostly constant, i.e., the rms of their V-band observations from the ASAS-SN Photometry Database ([Shappee et al. 2014](#); [Jayasinghe et al. 2019](#)) were below 0.1 mag. The APASS9 catalog provided Bessell *BV* and Sloan *g'r'i'* magnitudes for the comparison stars. We used the comparison stars for the photometric calibration by fitting a linear color term. Magnitudes taken with the same filter on the same night were averaged. The final uncertainties are the quadratic sum of the formal uncertainties of the aperture photometry, the photometric calibration, and the scatter of the individual magnitudes that were averaged per night. The results can be found in Tab. A1 in the Appendix. As seen in Fig. 1, Gaia20fgx is close to a very bright star, however, given the used aperture, and that the separation between Gaia20fgx and the bright star is $\sim 7''$, the results from the photometry were not affected by this nearby source.

We obtained near-infrared photometric observations in the *J*, *H* and *K_s* bands of Gaia20bwa on 2021 February 11 and Gaia20fgx on 2021 January 27. We used the Near Infrared Camera Spectrometer (NICS) instrument on the Telescopio Nazionale Galileo (TNG) located in the Island of San Miguel de La Palma (Canary Islands, Spain), proposal ID: AOT42, PI: Eleonora Fiorellino. In each filter a 5-point dithering was performed, with 3 s of exposure time at each position. The data reduction, performed with our own IDL routines, included the construction and subtraction of a sky image, and flat-fielding. On 2021 September 18, we obtained additional *JHK_s* photometry of Gaia20fgx from the Gran Telescopio Canaria (GTC) using the Espectrógrafo Multiobjeto Infra-Rojo (EMIR) instrument ([Balcells et al. 2000](#)), proposal ID: GTC01-21BDDT, PI: David García. The images were obtained in four dither positions with $10''$ offsets with 5 s exposure per dither point. These data were processed using the PyEMIR ([Pascual et al. 2010](#)) pipeline version 0.163. For photometric calibration of the TNG and GTC photometry, the 2MASS catalog was adopted. We extracted the instrumental magnitudes for the target as well as for all good-quality 2MASS stars (i.e. with a 2MASS photometric quality flag of AAA) in the field in an aperture with a radius of $\sim 1.5''$. The final step was the determination of an average constant calibration factor between the instrumental and the 2MASS magnitudes of typically 30 – 50 stars, and this offset was applied on the target observations. The formal photometric uncertainties are $0.01 - 0.02$ mag for the TNG data and $0.07 - 0.14$ for the GTC data. The results can be found in Tab. A1 in the Appendix.

We also used mid-infrared photometry from the Wide-field Infrared Survey Explorer (*WISE*) and *NEOWISE* surveys from the

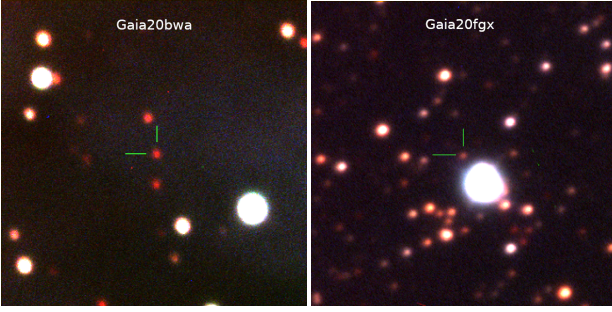


Figure 1. $Vr'i'$ color composite images of Gaia20bwa (left) and Gaia20fgx (right). The images show $3' \times 3'$ areas centered on the targets. North is up, east is to the left.

NASA/IPAC Infrared Science Archive. *NEOWISE* observes the full sky on average twice per year with multiple exposure per epoch. For a comparison with the photometry from other instruments, we computed the average and standard deviation of multiple exposures of a single epoch. The error bars are a quadratic sum of the average magnitude uncertainty per exposure. We downloaded G band photometry from the *Gaia* Science Alerts Index website. We also used r and g band photometry from the Data Release 11 of the Zwicky Transient Facility (ZTF; Masci et al. 2019).

2.2 Optical spectroscopy

We used the TNG equipped with the Device Optimized for the Low REsolution (Dolores) to obtain low-resolution optical spectra of Gaia20bwa on 2021 February 11/12, and Gaia20fgx on 2021 January 27/28. The UV-NIR coverage was achieved using the LRB and LRR gratings, which operate in $\sim 3500\text{--}7980$ and $\sim 4980\text{--}10370$ Å spectral ranges, respectively. The spectra were reduced in a standard way on bias, flatfield and then wavelength-calibrated within IRAF. The strong fringing pattern (apparent above 7800 Å) was successfully removed by normalized flatfield division. This worked only for the Gaia20bwa spectrum, the same procedure failed for the second star. This appears to have been caused by the low elevation at which the telescope was pointing during the observation of Gaia20fgx, at an airmass range 2.5 – 2.7, resulting in increased instrumental flexures distorting the nominal optical path. We averaged the overlapping part of LRB and LRR ranges assuming weights appropriate to the obtained signal. In addition, we observed Gaia20bwa on 2021 February 17/18 using the 2-m Liverpool Telescope (LT) equipped with the SPectrograph for the Rapid Acquisition of Transients (SPRAT, Piascik et al. 2014)¹. SPRAT provides low-resolution ($R=350$) spectra in the range of 4020 – 7994 Å. The spectrum was reduced and approximately calibrated to absolute flux units by means of the dedicated SPRAT pipeline. The spectral resolutions and total integration times corresponding to the optical spectra are listed in Table 1.

2.3 NIR spectroscopy

Low resolution ($R=500\text{--}1250$) NIR spectra were obtained with the Near Infrared Camera Spectrometer (NICS, Baffa et al. 2001) installed on the TNG on 2021 February 11 for Gaia20bwa and on 2021 January 27 for Gaia20fgx. For Gaia20bwa the J , HK , and K_b bands were used with exposure times of 1000 s, 120 s, and 520 s,

respectively. For Gaia20fgx, the IJ , HK , and K_b bands were used with exposure times of 2000 s, 400 s, and 1400 s, respectively. The sources were observed through the $1''$ wide slit. The data were reduced using IRAF. For each image, sky subtraction, flat-fielding, bad pixel removal, aperture tracing, and wavelength calibration (using argon lamp) were performed. Then, the telluric correction was performed: the hydrogen absorption lines in the telluric stellar spectrum were removed by Gaussian fitting, and the telluric spectrum was normalized. Subsequently we divided the target spectrum by the normalized telluric spectrum. The barycentric velocity was calculated by barycorrpy (Kanodia & Wright 2018) as -23.22 and -15.14 km s⁻¹ for Gaia20bwa and Gaia20fgx, respectively, and then subtracted from the target spectra. Finally, after normalizing the telluric corrected target spectrum, flux calibration was performed by using our photometry from Mt. Suhora and the TNG during the bright state, and the *WISE* W1 and W2 photometry close to the bright state for Gaia20bwa. For Gaia20fgx, faint states of *WISE* data are used in addition to bright states of optical to NIR.

We obtained medium-resolution ($R=4000\text{--}5000$) spectra for Gaia20fgx in JHK_s -bands on 2021 September 19, using the GTC equipped with EMIR configured in the long-slit mode (PI: D. García). The star was observed through the $0''.8$ wide slit. The total exposure times were 7174 s in the J , 2795 s in the H , and 3235 s in the K_s band. HgAr lamp provided wavelength calibration. The spectra were obtained in ABBA nodding pattern along the slit and were processed by means of the dedicated PyEMIR package. The final spectrum extraction was performed under IRAF. The telluric correction was done using the telluric standard HD 212495. We calibrated these spectra to absolute flux using the JHK_s band photometry obtained on the same night. The spectral resolutions and total integration times corresponding to the NIR spectra are listed in Table 1.

3 RESULTS

3.1 The distance of Gaia20fgx

While the distance of Gaia20bwa is accurately known, the distance of Gaia20fgx ($1.01^{+1.88}_{-0.32}$ kpc, Bailer-Jones et al. 2021) has a large uncertainty. Based on its position, proper motion, and its distance, Gaia20fgx belongs to the Cep OB3 association. To derive its more accurate distance, we collected the list of sources, which also belong to the Cep OB3 association (Jordi et al. 1996, Getman et al. 2009), and downloaded their Gaia EDR3 distances from Bailer-Jones et al. (2021). We considered only those sources, that had a Renormalised Unit Weight Error (RUWE) below 1.4. We removed the sources with a negative parallax from our sample, and those, where the parallax was less than five times its error. After applying these selection criteria, the number of sources used for the analysis is 235. The number of sources per photogeometric distance in 10 pc bins is shown in Fig. 2. Based on a Gaussian fit, the distribution of distances peaks at ~ 816 pc. The FWHM of the Gaussian fit is ~ 124 pc. We use the Gaussian sigma of $\sigma = FWHM/2.355 = 52.7$ pc as the error of the distance. Based on this analysis, the distance of Cep OB3 is $\sim 816 \pm 53$ pc. We will use this value when calculating physical parameters for Gaia20fgx in the next sections.

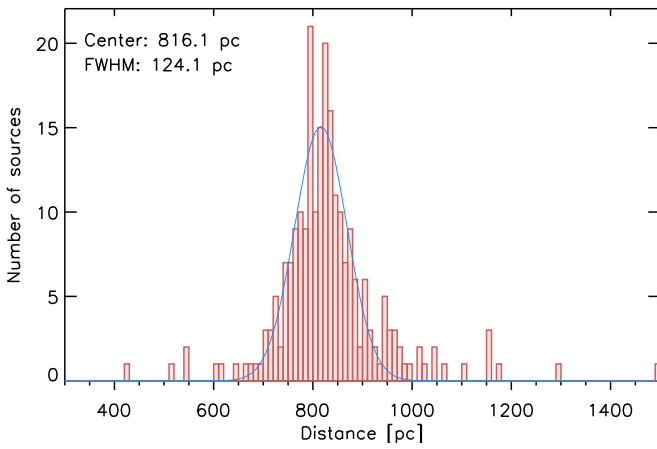
3.2 Light curves

Gaia and *WISE* light curves of Gaia20bwa and Gaia20fgx are shown in Fig. 3. For Gaia20fgx we also show data from the Zwicky Transient

¹ ProgID: XOL20B01, PI: Pawel Zielinski

Table 1. Log of spectroscopic observations.

Target	Date	Telescope	Instrument	Wavelength (μm)	Resolution	Total int. time (s)
Gaia20fgx	2021 Jan 27	TNG	DOLORES	0.59–1.00	585–714	1700
Gaia20fgx	2021 Jan 27	TNG	NICS	0.90–1.45	500	8000
Gaia20fgx	2021 Jan 27	TNG	NICS	1.40–2.50	500	1600
Gaia20fgx	2021 Jan 27	TNG	NICS	1.95–2.34	1250	5600
Gaia20fgx	2021 Sep 19	GTC	EMIR	1.17–1.33	4000–5000	7174
Gaia20fgx	2021 Sep 19	GTC	EMIR	1.53–1.78	4000–5000	2795
Gaia20fgx	2021 Sep 19	GTC	EMIR	2.03–2.38	4000–5000	3235
Gaia20bwa	2021 Feb 17	LT	SPRAT	0.40–0.80	350	200
Gaia20bwa	2021 Feb 11	TNG	DOLORES	0.59–1.00	585–714	630
Gaia20bwa	2021 Feb 11	TNG	NICS	1.12–1.40	1200	4000
Gaia20bwa	2021 Feb 11	TNG	NICS	1.40–2.50	500	480
Gaia20bwa	2021 Feb 11	TNG	NICS	1.95–2.34	1250	2080

**Figure 2.** Histogram of *Gaia* EDR3 distances of the members of the Cep OB3 region in 10 pc bins. The fitted Gaussian peaks at a value of ~ 816 pc.

Facility (ZTF) archive². For Gaia20bwa, we did not consider the ZTF data, due to the quality of the photometry in the ZTF Data Release 11: most of the data points are defined as bad-quality.

Gaia20bwa had a *Gaia* alert on 2020 April 17, when its brightness increased by about 0.3 mag in the *Gaia* *G*-band. It continued brightening by about 0.2 mag to reach its maximum brightness in 2020 October. The last *WISE* data point also follows the brightening seen in the *Gaia* light curve. Based on the *Gaia* light curve as well as our follow-up photometry with the RC80, Gaia20bwa faded back to its long-term brightness by the end of 2021 August, therefore, the brightening episode lasted for approximately 17 months.

Gaia20fgx had a *Gaia* alert on 2020 November 11, due to its brightening by ~ 2.5 mag over about 10 months. It reached its maximum brightness by 2021 February, and returned to quiescence by 2022 May, based on the *G*-band data. The *Gaia* light curve also shows an earlier brightening from early 2018 until early 2019, with a lower amplitude compared to the second brightening that corresponds to the *Gaia* alert. In addition to the two long-term brightening events, shorter brightenings with an amplitude of ~ 1 mag are apparent on the *Gaia* light curve between 2015 and 2018.

3.3 Color variations

Figure 4 shows the $(J - H)$ versus $(H - K_S)$ color-color diagram of the sources. Gaia20bwa is close to the locus of unreddened CTTS based on each three data points, and in both the bright and faint states. This suggests that the visual extinction for Gaia20bwa is low, however, we will use the SEDs in Sect. 3.5 to constrain the A_V for Gaia20bwa. For Gaia20fgx, there is evidence for a change in the visual extinction between the faint state represented by the 2MASS data point and the bright state represented by the TNG data point, while the GTC photometry corresponds to the fading of the source, between the bright and faint states. Gaia20fgx was redder at the 2MASS epoch, than at the later epochs observed with the TNG and the GTC. For Gaia20fgx, we used the expression from Cardelli et al. (1989) to measure the visual extinction of the source at each epoch by projecting its location in Fig. 4 to the line representing the locus of unreddened CTTS (Meyer et al. 1997) along the extinction path. This method results in an $A_V = 3.6 \pm 0.2$ mag for the bright state and 5.7 ± 0.6 mag for the faint state, when assuming an R_V of 3.1. An $A_V = 4.1 \pm 0.2$ mag was found for the GTC data point.

Color-magnitude diagrams based on the *WISE* data are shown in Fig. 5. There is no significant color change in the case of Gaia20fgx. For Gaia20bwa, the *W2* versus *W1*–*W2* color-magnitude diagram suggests reddening during the brightening, which is likely due to the disk component.

Figure 5 also shows a g vs. $[g - r]$ color-magnitude diagram for Gaia20fgx based on archival data from the ZTF survey and our follow-up observations with the RC80 and Mt. Suhora telescopes. Some of the data points indicate color-variations related to changing extinction. Both brightening events seen in Fig. 5 based on the g vs. $[g - r]$ color-magnitude diagram show a linear color variation over time: the red-orange data points correspond to the first brightening event, while the blue data points to the brightening related to the *Gaia* alert. The data points corresponding to the second brightening event seem to follow the extinction path. The r versus $[r - i]$ color-magnitude diagram shown in Fig. 5 for Gaia20bwa based on data points during the bright state and the fading shows a linear trend, however, it is not consistent with the extinction path. It suggests that the fading was caused by a mechanism other than variable extinction.

3.4 Results from spectroscopy

Due to the low spectral resolution of the TNG and LT spectra, the velocities of the lines cannot be accurately determined. However, the

² <https://irsa.ipac.caltech.edu/Missions/ztf.html>

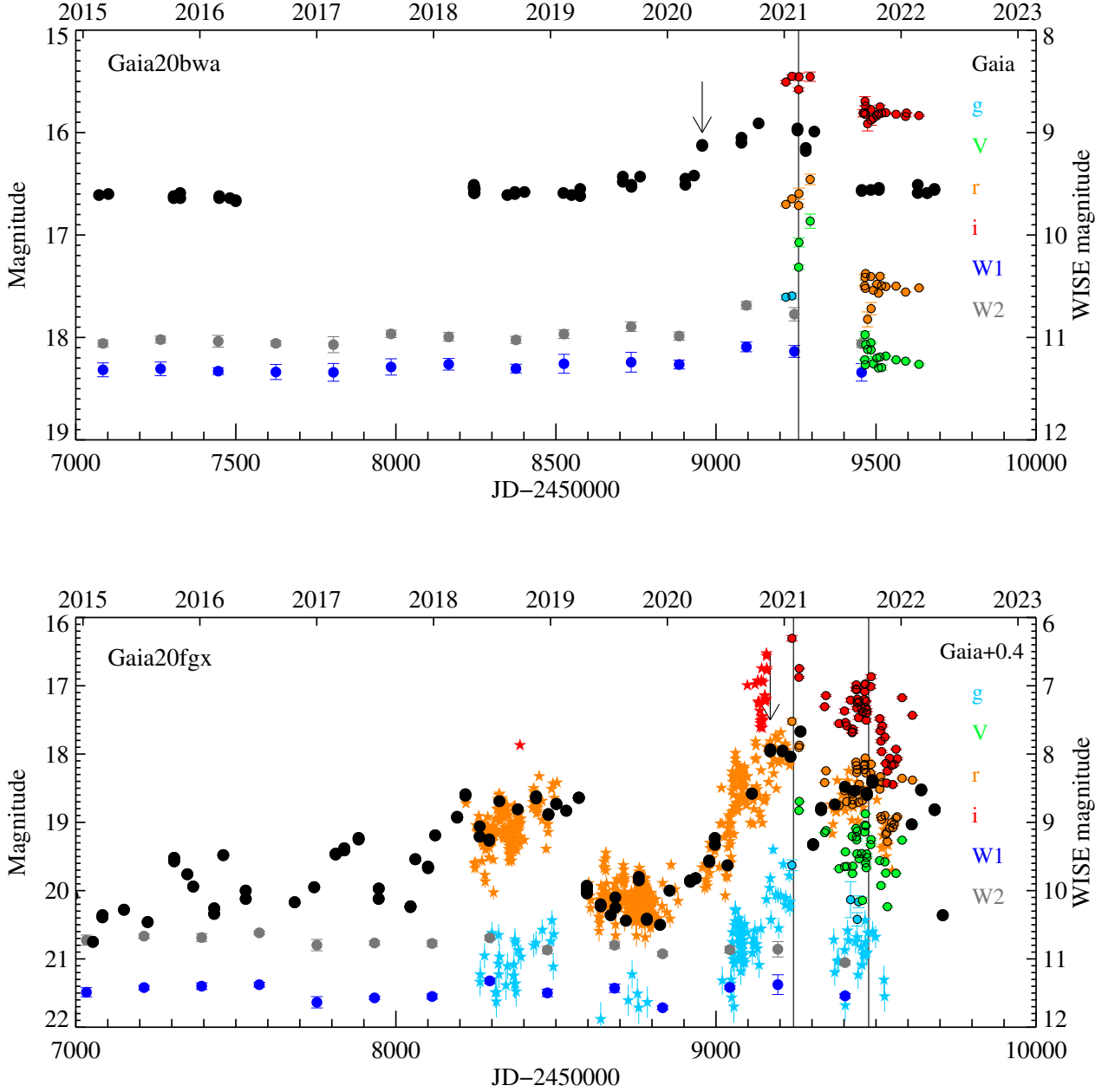


Figure 3. Light curves of Gaia20bwa and Gaia20fgx. The *Gaia* G data are shown with black dots, the ZTF *g*, *r*, and *i* data with light blue, orange, and red asterisks, the *WISE* W1 and W2 band data with blue and grey dots. The red, orange, and green dots are *i*, *r*, and *V* data measured with the RC80 or the Mt. Suhora telescope, as shown in Appendix A. The vertical lines show the epochs of the TNG and GTC spectra. The arrows show the epochs of the *Gaia* alerts.

equivalent widths and fluxes of the lines can be measured and used as tracers of characteristics of the sources, such as the accretion rate.

Several lines were detected in the optical spectrum of Gaia20bwa measured with the TNG, including lines from the H I Balmer series from H α to H δ , the Na I D line, the O I triplet at 7771/4/5 Å, the O I line at 8446 Å, and three lines of Ca II (Fig. 6). The H I Balmer series from H α to H γ were also detected in the spectrum taken with the LT. The Br γ and Pa β lines were detected in the NIR spectrum obtained with the TNG.

Due to the lower S/N of the fainter Gaia20fgx, only the H α line of the H I Balmer series was detected in the optical spectra measured with both the TNG and LT. The Br γ line was detected in the NIR spectrum observed with the TNG. A few additional lines were also detected in the medium resolution spectrum obtained with the GTC during the fading of the source: the CO 2-0 and 3-1 bandhead features in absorption, and the Pa β line detected as an inverse P Cygni profile (Fig. 7). The line parameters obtained from Gaussian fitting are shown in Table 2.

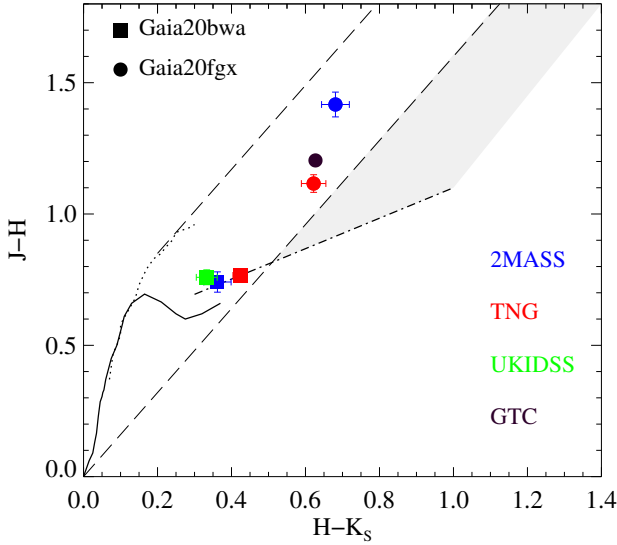


Figure 4. $(J - H)$ versus $(H - K_s)$ color-color diagram. The filled circles correspond to Gaia20fgx, the squares to Gaia20bwa. The blue symbols show 2MASS data, the red points TNG data, and the green symbol is from the UKIRT Infrared Deep Sky Survey (UKIDSS). The solid curve shows the colors of the zero-age main-sequence, and the dotted line represents the giant branch (Bessell & Brett 1988). The long-dashed lines delimit the area occupied by the reddened normal stars (Cardelli et al. 1989). The dash-dotted line is the locus of unreddened CTTS (Meyer et al. 1997) and the grey shaded band borders the area of the reddened K_s -excess stars.

Detecting several lines of the Balmer series for Gaia20bwa allows us to determine the excitation temperature of the gas that emits these lines. In Fig. 8 we plotted the line fluxes divided by the statistical weights of the energy levels in logarithmic scale as a function of the energy of the levels and applied a linear fit to the data points. The inverse of the slope of the lines gave an excitation temperature of ~ 7600 K for both the TNG and LT data. This value is higher than the photospheric temperature of CTTS, as well as the 3142.5 ± 16.0 K effective temperature derived for Gaia20bwa (Da Rio et al. 2016), indicating that the detected hydrogen lines originate from gas participating in the accretion process, located close to the magnetospheric hotspot, or residing in the accretion column. However, the ~ 7600 K temperature derived above is an upper limit, given that Balmer lines emitted in the accretion columns are likely to be optically thick.

We can use the ~ 7600 K temperature derived above to interpret the trend seen in the r versus $[r-i]$ color-magnitude diagram (Fig. 5). Large amplitude optical brightness variations in CTTS in the optical regime can be produced by variations of photospheric hot spots, resulting from variable accretion rates (Carpenter et al. 2001; Scholz et al. 2009). We applied the method described by Scholz et al. (2009) to model the brightness and color variations of Gaia20bwa during the fading. We found that the amplitude and slope of the color-magnitude diagram can be reproduced by cooling of a hot spot covering some 1.5% of the stellar surface from a temperature of ~ 7600 K to the photospheric temperature.

3.5 SEDs and stellar parameters

The SEDs of Gaia20bwa and Gaia20fgx are shown in Fig. 9. The data points for the bright state (red symbols) are based on our follow-up observations with the TNG and Mt. Suhora telescopes, the *Gaia* G -

band data measured close to the TNG and Mt. Suhora observations, and on the last published *WISE* W1 and W2 fluxes. The data points for the faint state are based on archival data from Pan-STARRS, *Gaia*, *WISE*, 2MASS and *Spitzer*. We computed black body functions for a range of temperatures and visual extinctions and compared them to the SEDs by visual inspection. We used the temperature and A_V values estimated from the SEDs to derive stellar parameters for the sources. We explain the results for each source below.

3.5.1 Gaia20fgx

The SED of Gaia20fgx in the faint state is consistent with a temperature of 3700 ± 300 K and a visual extinction of $A_V = 7.0 \pm 0.7$ mag, which is slightly above the value that was derived for the faint state based on the $J - H$ versus $H - K_s$ plot, and is consistent with the ~ 7.3 mag value derived by Chen et al. (2020). Similarly, the SED in the bright state is more consistent with a higher A_V compared to the value derived from the $J - H$ versus $H - K_s$ plot, with an A_V of 5 ± 0.5 mag. The 3700 K temperature is between the M0 and M1 spectral types (Pecaut & Mamajek 2013). The luminosity of Gaia20fgx can be derived from the observed magnitudes corrected for extinction and assuming a bolometric correction (BC). We used the bolometric correction value corresponding to the average of the values for the M0 and M1 spectral types in the J band (BC_J) of 5-30 Myr stars from Table 6 of Pecaut & Mamajek (2013). The luminosity of Gaia20fgx is then

$$\log \left(\frac{L_\star}{L_\odot} \right) = 0.4(M_{\text{bol},\odot} - M_{\text{bol}}), \quad (1)$$

where $M_{\text{bol},\odot}$ is the bolometric magnitude of the Sun (Mamajek et al. 2015), and the bolometric magnitude of the source is $M_{\text{bol}} = m_J - 5 \log(d/10[\text{pc}]) + BC_J$ where m_J is the extinction corrected J magnitude of 12.57 ± 0.03 mag (assuming an $A_V = 7$ mag). This results in $L_\star = 1.02 \pm 0.20 L_\odot$ for Gaia20fgx. Based on the L_\star and T_{eff} derived above and the evolutionary tracks by Siess et al. (2000), we determined a stellar mass of $M_\star = 0.53 \pm 0.10 M_\odot$. Assuming that the central object emits as a black-body, the stellar radius can be derived as

$$R_\star = \frac{1}{2T_{\text{eff}}^2} \sqrt{\frac{L_\star}{\pi\sigma}} \quad (2)$$

where σ is the Stefan-Boltzmann constant. The R_\star for Gaia20fgx is $2.46 \pm 0.52 R_\odot$ using this method. The stellar parameters derived for Gaia20fgx in the faint and bright states are summarized in Table 3.

3.5.2 Gaia20bwa

The SED of Gaia20bwa in the faint state is consistent with a temperature of 3300 ± 200 K and a visual extinction of $A_V = 3.0 \pm 0.5$ mag. This temperature is consistent with the 3142.5 ± 16.04 K derived by Da Rio et al. (2016), but the derived A_V value is above the 0.9 ± 0.35 mag suggested by Da Rio et al. (2016). These parameters (3300 K temperature and 3.0 mag visual extinction) are also consistent with SED in the bright state. A temperature of 3300 K is close to the M3 spectral type (Pecaut & Mamajek 2013). We used the bolometric correction value corresponding to the M3 spectral type in the J band (BC_J) of 5-30 Myr stars from Table 6 of Pecaut & Mamajek (2013). The extinction corrected J magnitude is 12.03 ± 0.03 mag (assuming an $A_V = 3.0$ mag). Using Eqn. 1, we derived a luminosity of $0.38 \pm 0.06 L_\odot$. Based on the L_\star and T_{eff} derived above and the evolutionary tracks by Siess et al. (2000), we determined a stellar

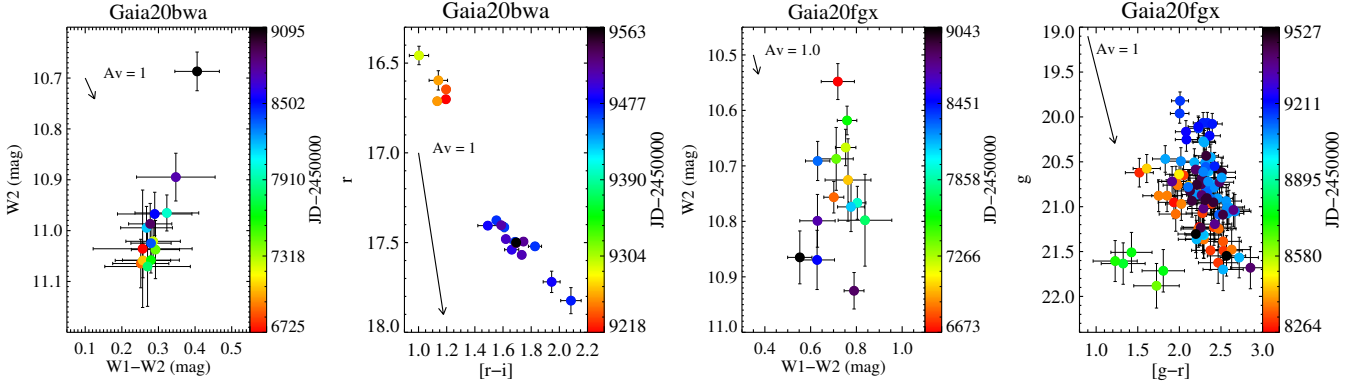


Figure 5. *Left panels:* Color-magnitude diagrams of Gaia20bwa based on data from *WISE* and from the RC80 telescope. *Right panels:* Color-magnitude diagrams of Gaia20fgx based on data from *WISE* and follow-up photometry in *g* and *r* bands. The *g* versus $[g - r]$ color-magnitude diagrams are based on data from the ZTF survey as well as from the RC80 and Mt. Suhora telescopes as shown in Table A.1. We only used those ZTF data points, when both *g* and *r* magnitudes were measured during the same night.

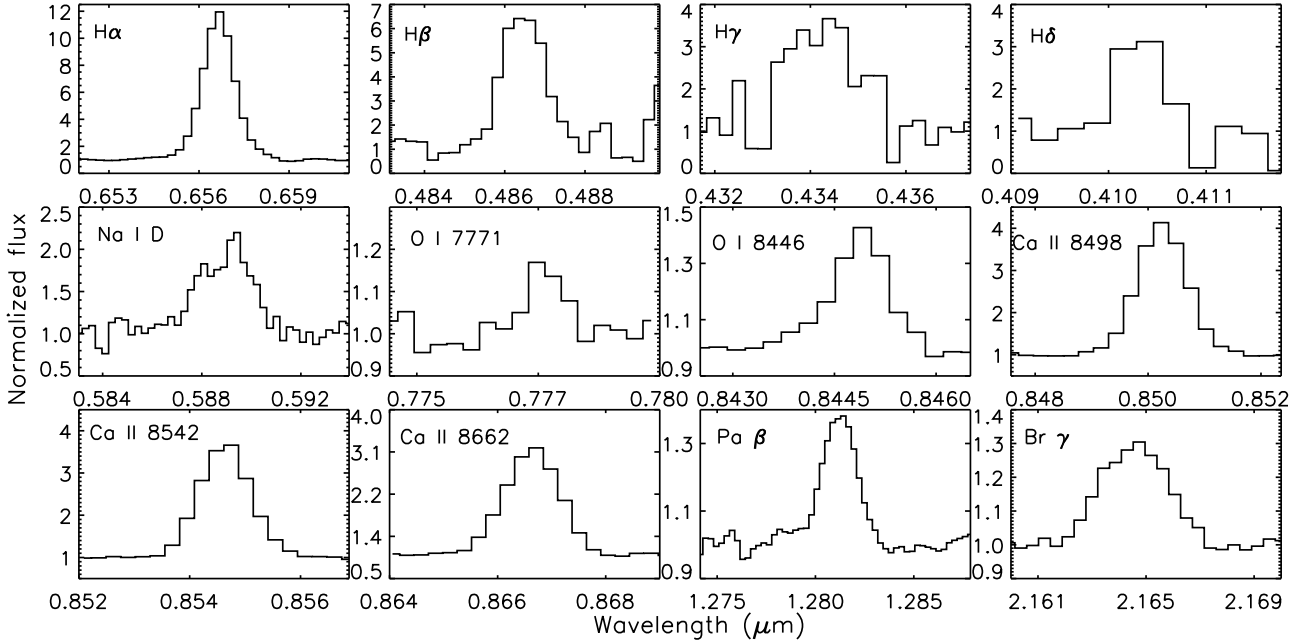


Figure 6. Lines detected toward Gaia20bwa in optical (using TNG/DOLores) and NIR (using TNG/NICS).

mass of $M_{\star} = 0.28 \pm 0.06 M_{\odot}$. Using Eqn. 2, we derived a radius of $1.89 \pm 0.32 R_{\odot}$. The stellar parameters derived for Gaia20bwa are summarized in Table 3. The temperature, A_V , L_{\star} , and M_{\star} derived for Gaia20bwa by Da Rio et al. (2016) are also listed in Table 3. The R_{\star} corresponding to these parameters was derived using Eqn. 2 based on the temperature and luminosity from Da Rio et al. (2016). Although the temperature derived here for Gaia20bwa is consistent with the value derived by Da Rio et al. (2016) within the uncertainties, the stellar luminosity, mass, and radius derived here are about factors of 2, 1.4, and 1.3 larger, respectively. The difference between the stellar parameters derived here and by Da Rio et al. (2016) is mostly due to the higher visual extinction we found from the SED fit.

3.6 Accretion rates

The line fluxes shown in Table 2 can be converted to line luminosities as $L_{\text{line}} = 4\pi d^2 f_{\text{line}}$, where d is the distance of the sources, and f_{line} is the extinction-corrected flux of the lines. For the accretion parameters derived in this Section, we use the visual extinctions estimated from the SEDs when available, rather than the values derived from the $J - H$ versus $H - K_s$ plot. The SEDs allow to better constrain the visual extinctions than three data points (the J , H , and K_s magnitudes). The accretion parameters derived from the different lines also confirm this, as they are more consistent when derived using the visual extinctions estimated from the SED, rather than from the $J - H$ versus $H - K_s$ plot. The visual extinctions derived from the SEDs in the bright state are 3 mag for Gaia20bwa and 5 mag for Gaia20fgx, while in the faint state they are 3 mag and 7 mag, respectively. For

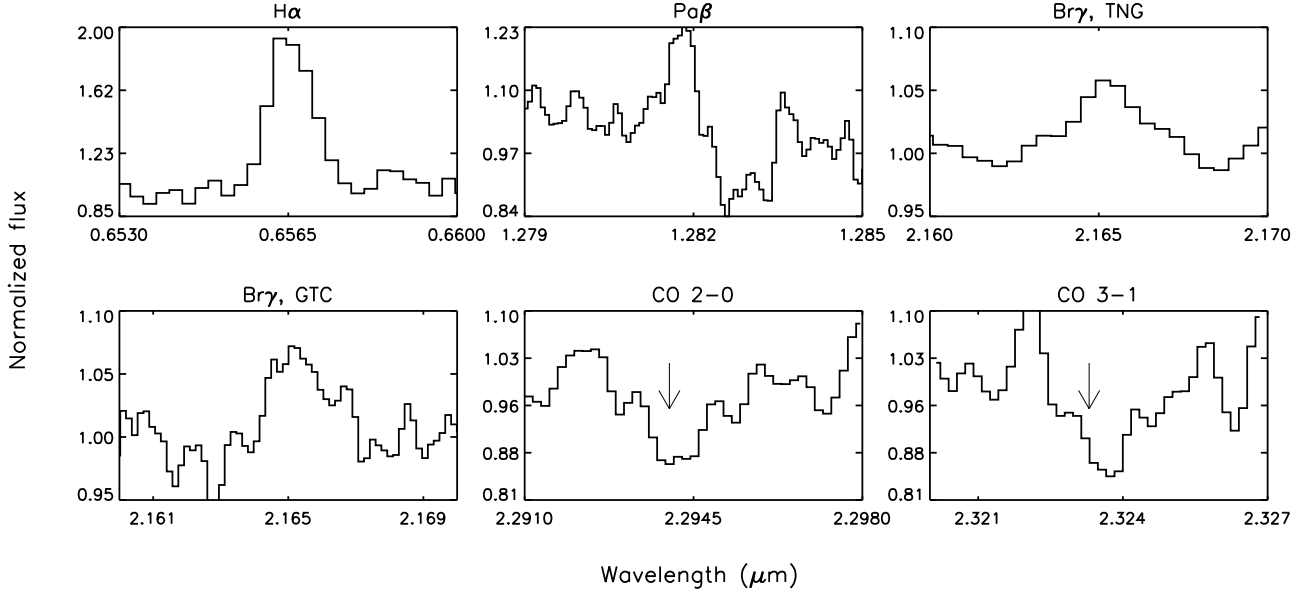


Figure 7. Lines detected toward Gaia20fgx (using TNG/DOLORES and NICS and GTC/EMIR).

Table 2. Parameters of the lines detected toward Gaia20bwa and Gaia20fgx.

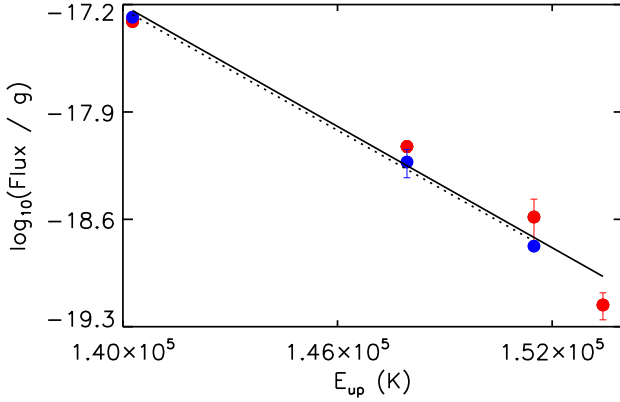
Line	Telescope	Center (Å)	EW (Å)	FWHM (Å)	f_{line} (W/m ²)
Gaia20bwa					
H α	TNG	6567.3 \pm 0.3	-153.6 \pm 10	12.3 \pm 0.4	(8.8 \pm 1.3) $\times 10^{-17}$
H α	LT	6567.8 \pm 0.1	-152 \pm 6	13.8 \pm 0.1	(9.4 \pm 1.4) $\times 10^{-17}$
H β	TNG	4863.3 \pm 1.5	-58 \pm 5	12.6 \pm 1.0	(2.4 \pm 0.6) $\times 10^{-17}$
H β	LT	4866.1 \pm 0.1	-108 \pm 7	14.5 \pm 0.1	(1.9 \pm 0.4) $\times 10^{-17}$
H γ	TNG	4342.4 \pm 2.4	-46.4 \pm 9.5	16.0 \pm 2.0	(1.3 \pm 0.7) $\times 10^{-17}$
H γ	LT	4341.1 \pm 0.3	-31.8 \pm 2	15.2 \pm 0.1	(8.4 \pm 2.5) $\times 10^{-18}$
H δ	TNG	4103.1 \pm 0.8	-19.2 \pm 5	6.5 \pm 1.9	(5.0 \pm 2.5) $\times 10^{-18}$
Ca II	TNG	8502.3 \pm 0.1	-31.3 \pm 2.9	10.9 \pm 1.3	(4.4 \pm 0.9) $\times 10^{-17}$
Ca II	TNG	8546.6 \pm 0.3	-30.8 \pm 2	11.4 \pm 1.0	(4.3 \pm 0.9) $\times 10^{-17}$
Ca II	TNG	8666.2 \pm 0.6	-29.2 \pm 1.3	11.7 \pm 0.8	(4.4 \pm 0.9) $\times 10^{-17}$
O I	TNG	7775.3 \pm 0.3	-0.9 \pm 0.1	6.2 \pm 0.5	(1.0 \pm 0.5) $\times 10^{-18}$
O I	TNG	8449.0 \pm 0.7	-2.7 \pm 0.8	7.6 \pm 1.6	(3.5 \pm 1.4) $\times 10^{-18}$
Na I D	TNG	5893.3 \pm 0.4	-5.7 \pm 0.6	6.2 \pm 0.5	(3.8 \pm 1.9) $\times 10^{-18}$
Na I D	TNG	5900.5 \pm 0.1	-4.9 \pm 0.3	4.3 \pm 0.1	(4.1 \pm 2.1) $\times 10^{-18}$
Pa β	TNG	12812 \pm 1	-8.5 \pm 0.5	13.5 \pm 0.5	(1.4 \pm 0.5) $\times 10^{-17}$
Br γ	TNG	21647 \pm 2	-13.7 \pm 0.3	23 \pm 1	(8.8 \pm 3.1) $\times 10^{-18}$
Gaia20fgx					
H α	TNG	6564.8 \pm 2	-12.3 \pm 1	10 \pm 2	(4.0 \pm 0.8) $\times 10^{-18}$
Br γ	TNG	21683 \pm 4	-10 \pm 1	48 \pm 6	(4.0 \pm 2.0) $\times 10^{-18}$
Br γ	GTC	21652 \pm 1	-1.4 \pm 0.2	20 \pm 3	(7.0 \pm 2.1) $\times 10^{-19}$

the estimate based on the Br γ line observed with the GTC, we used the extinction of ~ 4.1 mag derived from the $J - H$ versus $H - K_s$ plot. However, we found, that the SEDs suggest 20-30% higher visual extinctions compared to the $J - H$ versus $H - K_s$ plot. Therefore, to be consistent with the A_V values derived from the SEDs, we used a value of 5.5 mag for the GTC data, a 25% higher value than derived from the $J - H$ versus $H - K_s$ plot. For the extinction correction, we assumed an R_V of 5.5 for Gaia20bwa, as suggested by [Da Rio](#)

[et al. \(2016\)](#) as an average value for the Orion A cloud, while we assumed an R_V of 3.1 for Gaia20fgx. However, this does not make a significant difference in the derived accretion parameters, and affects the accretion parameters by $\sim 10\%$ or less. For the distance of Gaia20bwa we adopted 410^{+12}_{-11} pc ([Bailer-Jones et al. 2021](#)), while for the distance of Gaia20fgx we assumed the $\sim 816 \pm 53$ pc derived in Sec. 3.1 for the distance of Cep OB3. We derived the accretion luminosities from the line luminosities based on the relations pro-

Table 3. Summary of the stellar parameters of Gaia20bwa and Gaia20fgx.

	T (K)	A_V (mag)	L_\star (L_\odot)	M_\star (M_\odot)	R_\star (R_\odot)
Gaia20bwa faint & bright states	3300 ± 200	3.0 ± 0.5	0.38 ± 0.06	0.28 ± 0.06	1.89 ± 0.32
Gaia20bwa based on Da Rio et al. (2016)	3142.5 ± 16.04	0.9 ± 0.35	0.20 ± 0.02	0.206 ± 0.008	1.51 ± 0.15
Gaia20fgx faint state	3700 ± 300	7.0 ± 0.7	1.02 ± 0.20	0.53 ± 0.10	2.46 ± 0.52
Gaia20fgx bright state	3700 ± 300	5.0 ± 0.5	0.61 ± 0.12	0.47 ± 0.10	1.90 ± 0.40


Figure 8. Excitation diagram for the hydrogen Balmer lines of Gaia20bwa based on data from the TNG (red dots) and the Liverpool Telescope (blue dots). Some of the error bars are smaller than the symbol sizes. The solid line is the linear fit to the TNG data, while the dashed line is the fit to the LT data. Both lines result in a temperature of ~ 7600 K.

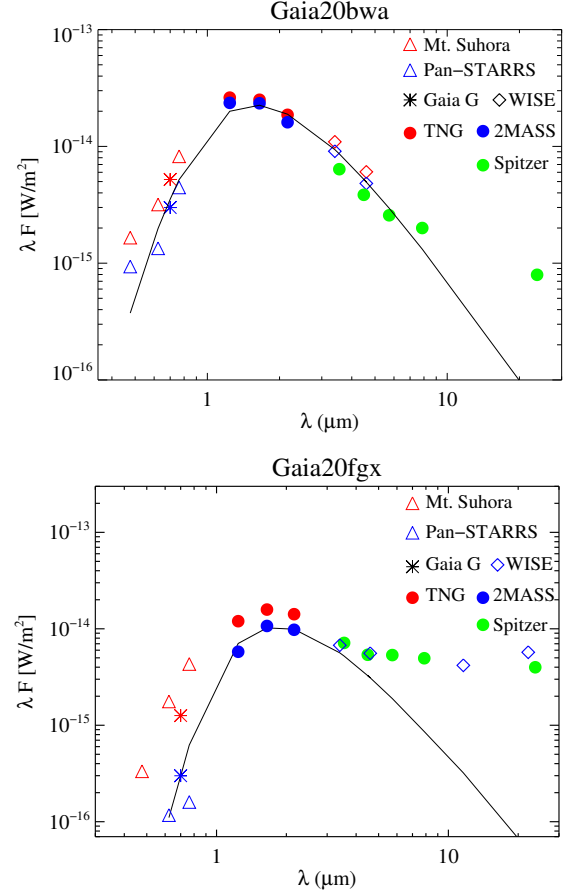
vided by Alcalá et al. (2017). The accretion luminosities can then be converted to accretion rates using the formula

$$\dot{M}_{\text{acc}} = 1.25 \frac{L_{\text{acc}} R_\star}{GM_\star}$$

for which an inner-disk radius of $5 R_\star$ was assumed (Hartmann et al. 1998). For Gaia20bwa, we used the radius of $1.89 \pm 0.32 R_\odot$ and stellar mass of $0.28 \pm 0.06 M_\odot$ derived above to provide one estimate of the accretion rates, and the radius of $1.51 \pm 0.15 R_\odot$ and stellar mass of $0.206 \pm 0.008 M_\odot$ for another estimate (Da Rio et al. 2016). For Gaia20fgx, we adopt the $R_\star = 2.46 \pm 0.52 R_\odot$ and $M_\star = 0.53 \pm 0.1 M_\odot$ values derived above for the faint state, and $R_\star = 1.90 \pm 0.40 R_\odot$ and $M_\star = 0.47 \pm 0.1 M_\odot$ values derived above for the bright state.

The accretion luminosities and rates are shown in Table 2 for both sets of stellar parameters from Table 3 for both sources. For the stellar parameters derived above for Gaia20bwa, the accretion luminosities are in the range between $(6.1 \pm 2.4) \times 10^{-2} L_\odot$ and $5.78 \pm 3.11 \times 10^{-1} L_\odot$, and the accretion rates are in the range between $(1.65 \pm 0.79) \times 10^{-8} M_\odot \text{ yr}^{-1}$ and $(1.60 \pm 0.9) \times 10^{-7} M_\odot \text{ yr}^{-1}$. Based on the stellar parameters from Da Rio et al. (2016), the accretion luminosities are in the range between $(1.64 \pm 0.85) \times 10^{-2} L_\odot$ and $(1.67 \pm 4.35) \times 10^{-1} L_\odot$, and the accretion rates are in the range between $(4.82 \pm 2.55) \times 10^{-9} M_\odot \text{ yr}^{-1}$ and $(4.89 \pm 13.78) \times 10^{-8} M_\odot \text{ yr}^{-1}$.

The accretion luminosities for Gaia20fgx during its bright state based on the TNG data are $(0.95 - 5.21) \times 10^{-1} L_\odot$ and $(2.77 - 3.58) \times 10^{-1} L_\odot$ based on the $H\alpha$ and the $\text{Br}\gamma$ lines, respectively, taking into account both sets of stellar parameters (Table 4). The accretion rates during the bright state are $(1.54 - 9.68) \times 10^{-8} M_\odot$


Figure 9. SEDs of Gaia20bwa and Gaia20fgx in the bright (red symbols) and faint (blue and green symbols) states. The overplotted black body curves correspond to a temperature of 3300 K and an A_V of 3 mag for Gaia20bwa, and a temperature of 3700 K and an A_V of 7 mag for Gaia20fgx.

yr^{-1} and $(4.48 - 6.64) \times 10^{-8} M_\odot \text{ yr}^{-1}$ based on the $H\alpha$ and the $\text{Br}\gamma$ lines, respectively. The accretion luminosity and rate derived for Gaia20fgx based on the $\text{Br}\gamma$ line measured with the GTC about half a year after the TNG measurements are almost a factor of 10 below those derived from the TNG data during the bright state. Since the $\text{Pa}\beta$ line detected with the GTC also has an absorption component, we did not use it to derive the accretion luminosity and rate.

4 DISCUSSION

4.1 The origin of the brightening events

Both targets show a brightening on a time-scale, which is typical of EXors (Herbig 1989, 2008). However, the amplitude of the bright-

Table 4. Accretion luminosities and rates for Gaia20bwa and Gaia20fgx. The accretion luminosities calculated from the fluxes based on [Alcalá et al. \(2017\)](#). For Gaia20bwa, $L_{\text{acc},1}$ and $\dot{M}_{\text{acc},1}$ correspond to the M_\star and R_\star values derived for the faint and bright states, while $L_{\text{acc},2}$ and $\dot{M}_{\text{acc},2}$ correspond to the M_\star and R_\star values derived by [Da Rio et al. \(2016\)](#). For Gaia20fgx, $L_{\text{acc},1}$ and $\dot{M}_{\text{acc},1}$ correspond to the M_\star and R_\star values derived for the faint state, and $L_{\text{acc},2}$ and $\dot{M}_{\text{acc},2}$ correspond to the M_\star and R_\star values derived for the bright state.

Line	Telescope	$L_{\text{acc},1}$ ($10^{-1} L_\odot$)	$\dot{M}_{\text{acc},1}$ ($10^{-8} M_\odot \text{ yr}^{-1}$)	$L_{\text{acc},2}$ ($10^{-2} L_\odot$)	$\dot{M}_{\text{acc},2}$ ($10^{-9} M_\odot \text{ yr}^{-1}$)
Gaia20bwa					
H α	TNG	1.36 \pm 0.30	3.68 \pm 1.29	2.09 \pm 0.46	6.14 \pm 1.50
H α	LT	1.47 \pm 0.32	3.97 \pm 1.39	2.25 \pm 0.49	6.61 \pm 1.60
H β	TNG	4.46 \pm 1.26	12.04 \pm 4.73	3.95 \pm 1.11	11.58 \pm 3.48
H β	LT	3.41 \pm 0.84	9.23 \pm 3.40	3.02 \pm 0.75	8.87 \pm 2.40
H γ	TNG	4.54 \pm 2.51	12.26 \pm 7.56	3.50 \pm 1.94	10.26 \pm 5.79
H γ	LT	2.79 \pm 0.90	7.55 \pm 3.19	2.15 \pm 0.70	6.32 \pm 2.17
H δ	TNG	2.13 \pm 1.10	5.74 \pm 3.35	1.64 \pm 0.85	4.82 \pm 2.55
Ca II	TNG	5.46 \pm 1.43	14.76 \pm 5.59	16.66 \pm 4.35	48.87 \pm 13.78
Ca II	TNG	4.07 \pm 1.10	11.00 \pm 4.23	12.84 \pm 3.48	37.66 \pm 10.97
Ca II	TNG	3.90 \pm 1.07	10.53 \pm 4.08	13.19 \pm 3.62	38.71 \pm 11.40
O I	TNG	1.07 \pm 0.57	2.90 \pm 1.74	1.90 \pm 1.00	5.56 \pm 2.99
O I	TNG	1.44 \pm 0.67	3.88 \pm 2.09	3.89 \pm 1.81	11.40 \pm 5.44
Na I D	TNG	3.46 \pm 1.83	9.35 \pm 5.57	5.46 \pm 2.88	16.02 \pm 8.62
Na I D	TNG	5.78 \pm 3.11	15.60 \pm 9.41	9.13 \pm 4.92	26.78 \pm 14.71
Pa β	TNG	0.61 \pm 0.24	1.65 \pm 0.79	3.17 \pm 1.26	9.31 \pm 3.83
Br γ	TNG	1.14 \pm 0.46	3.09 \pm 1.51	8.33 \pm 3.32	24.44 \pm 10.08
Gaia20fgx					
H α	TNG	5.21 \pm 1.40	9.68 \pm 3.78	9.50 \pm 2.55	15.37 \pm 6.18
Br γ	TNG	3.58 \pm 1.93	6.64 \pm 4.04	27.70 \pm 14.96	44.83 \pm 27.68
Br γ	GTC	0.37 \pm 0.13	0.70 \pm 0.32	3.71 \pm 1.35	6.01 \pm 2.83

ening for Gaia20bwa (~ 0.5 mag) is lower than expected for EXors, while the 2.5 mag brightening for Gaia20fgx is closer to that expected for EXors. In addition to the time-scale and amplitude of the brightening event reported as a *Gaia* alert for Gaia20fgx, it showed a brightening event earlier, between early 2018 and early 2019 (Fig. 3). Based on the currently available data, there is no evidence that the brightening of Gaia20bwa is also a recurring event. To understand the brightening events of the two targets, we compare their accretion parameters to those derived for other young stars.

The accretion luminosities versus the stellar luminosities as well as the accretion rates versus the stellar masses are plotted in Fig. 10. Samples of CTTS are also plotted for comparison toward the Lupus (black symbols, [Alcalá et al. 2019](#)), the Chamaeleon I (grey symbols, [Manara et al. 2019](#)), and the NGC 1333 (light blue symbols, [Fiorellino et al. 2021](#)) regions. The stellar luminosity of Gaia20bwa is close to the median value of the three samples, while its stellar mass is slightly below the median value of CTTS. Gaia20fgx is close to the most luminous end of the plotted CTTS, and its mass is above the median value of the plotted CTTS. While the accretion luminosities and rates for both Gaia20bwa and Gaia20fgx in their bright state are toward the upper end among CTTS with similar luminosities and masses, they still follow the trend seen in the accretion luminosity versus stellar luminosity and the accretion rate versus stellar mass in the CTTS samples. This is not the case for the few examples of EXors (triangles in Fig. 10), which are clearly above the general trends seen in the CTTS samples. One of the EXors plotted is the newly confirmed EXor corresponding to the *Gaia* alerted Gaia20eae ([Cruz-Sáenz de Miera et al. 2022](#)). The accretion luminosities and rates of the other EXors are from [Lorenzetti et al. \(2009\)](#). For UZ Tau E we used a stellar luminosity of $\sim 0.6 L_\odot$ and a mass of $\sim 1.0 M_\odot$ ([Prato et al. 2002](#)). For DR Tau we adopted a stellar luminosity of 0.87

L_\odot ([Muzerolle et al. 2003](#)), which, together with its K7 spectral type, corresponds to a stellar mass of $\sim 0.67 M_\odot$ ([Siess et al. 2000](#)). For V1118 Ori we adopted a stellar luminosity of $0.18 L_\odot$ and a stellar mass of $0.29 M_\odot$ ([Giannini et al. 2017](#)). For a better comparison, for Gaia20bwa, Gaia20fgx, and Gaia20eae ([Cruz-Sáenz de Miera et al. 2022](#)), and the EXors from [Lorenzetti et al. \(2009\)](#) we used the accretion luminosities and rates calculated from the Br γ line. Based on this comparison of the accretion versus stellar parameters, not only Gaia20bwa, but also Gaia20fgx is closer to CTTS than to EXors.

Brightness variations for young stars also occur due to a change of the circumstellar extinction, not only due to a change of the accretion rate. As seen in Fig. 5 in the g versus $[g-r]$ color-magnitude diagram of Gaia20fgx, the brightening event corresponding to the *Gaia* alert suggests a change in the visual extinction, such as suggested by the $J-H$ versus $H-K_s$ plot and the SEDs. To investigate how the accretion rate changes, we observed the NIR spectra of Gaia20fgx in its fading phase, about half a year after the first spectrum was taken in the bright state. The accretion rate derived from the Br γ line during the fading phase ($(6.01 - 7.0) \times 10^{-9} M_\odot \text{ yr}^{-1}$) is about a factor of 10 lower than during the bright state ($(4.48 - 6.64) \times 10^{-8} M_\odot \text{ yr}^{-1}$). This suggests, that while the visual extinction changed between the two epochs, the brightening event of Gaia20fgx corresponding to the *Gaia* alert was indeed due to an increase of the accretion rate, even if the increased accretion rate remained below the values expected for eruptive young stars. For Gaia20bwa, while there is only one estimate of its accretion rate, the color-color diagram in Fig. 4 indicates, that the visual extinction did not change significantly during the faint and the bright state. In addition to this, the brightening event was also seen in the WISE W1 and W2 bands. Therefore, the brightening event

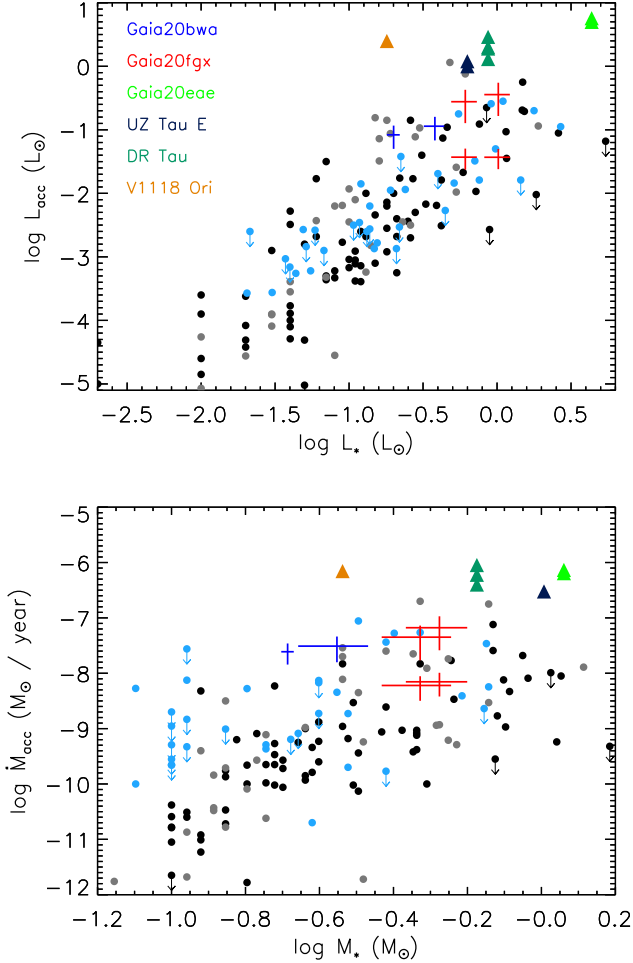


Figure 10. Accretion luminosities versus stellar luminosities (top panel), as well as accretion rates versus stellar masses (bottom panel) and their comparison to confirmed EXors (triangles) and samples of CTTS in the Lupus (black symbols, Alcalá et al. 2019), Chamaeleon I (grey symbols, Manara et al. 2019), and NGC 1333 (light blue symbols, Fiorellino et al. 2021) regions. The upper limits are marked with downward arrows.

for Gaia20bwa is likely also related to an increase of the accretion rate.

It was observed for several young eruptive stars, including Gaia17bpi (Hillenbrand et al. 2018) and Gaia18dvy (Szegedi-Elek et al. 2020), that their brightening occurs earlier at IR than at optical wavelengths. This phenomenon was found to be consistent with disk models that predict instabilities in the inner 0.5–1 au of accretion disks (Hillenbrand et al. 2018). Based on the *Gaia* and *WISE* light curves, there is no evidence of such behavior for either Gaia20bwa or Gaia20fgx, which supports the finding, that their brightenings are not related to instabilities like in the case of young eruptive stars.

4.2 The time-scale and amplitude of the brightening events

As discussed above from the comparison of the accretion rates, the sources studied here are most likely CTTS, rather than EXors. However, the brightness variations of CTTS typically occur on shorter time-scales than the brightenings of Gaia20bwa and Gaia20fgx, and

with lower amplitudes (Hillenbrand & Findeisen 2015). Though the brightening events with 0.5–2.5 mag amplitudes on a time-scale of a year or above are not typical of non-eruptive YSOs, a number of sources with variability on a similar time-scale were identified at NIR wavelengths (Contreras Peña et al. 2017). The sample of Contreras Peña et al. (2017) includes targets with $\Delta K_S > 1$ mag, out of which, several sources show long-term brightening, on a similar time-scale to Gaia20bwa and Gaia20fgx. However, given that the survey of Contreras Peña et al. (2017) was in the NIR, it cannot be directly compared to the *Gaia* light curves of Gaia20bwa and Gaia20fgx. The long-term variability of a sample of 72 CTTS based on optical photometry was analysed by Grankin et al. (2007), and though most of the sources in the sample showed a variability with an amplitude of $\Delta V \leq 0.4$ mag, there are a few sources with variability amplitudes up to $\Delta V \sim 2$ mag. Based on the long-term optical light curves of 218 CTTS, Briceño et al. (2019) found mean variability amplitudes of ~ 0.7 mag in the V-band and ~ 0.6 mag in the R-band, which are close to the ~ 1 mag variability, that is seen for Gaia20fgx between 2015 and 2018. The information on long-term brightness variations of YSOs is limited. Databases from photometric surveys, such as the *Gaia* Science Alerts, are expected to provide more information on brightenings of young stars on a time-scale of months-years.

4.3 Spectral properties of the sources

The lines identified in the spectra of both sources are also typical of EXors (Cruz-Sáenz de Miera et al. 2022 and references therein). However, the number of lines detected in the spectra is below what is typical of EXors, even when observed at low spectral resolution (Lorenzetti et al. 2009). For Gaia20fgx, the low number of detected lines in the spectra, in addition to the low spectral resolution, may also be related to its low brightness even during its bright state, when the TNG spectra were observed, and during its fading, when the GTC spectra were observed. As a comparison with a known EXor, the prototype EX Lupi, we plotted in Fig. 11 the TNG spectra of Gaia20bwa and Gaia20fgx together with those of EX Lupi. We used the spectra obtained during its latest, 2022 outburst (Kóspál et al. 2022), as its amplitude was $\lesssim 2$ mag in the *g* band (Ábrahám et al., in prep.), and as a less luminous outburst compared to the extreme eruption of EX Lupi in 2008 (Ábrahám et al. 2009), it provides a good comparison with our targets. Since these spectra were taken using VLT/XSHOOTER (Ábrahám et al., in prep.), we smoothed them to match their resolution to our low-resolution spectra. Several spectral lines are detected in the spectra of both Gaia20bwa and EX Lupi, e.g. the Balmer lines, Pa β , Br γ . However, several lines, which were detected in the spectrum of EX Lupi, such as lines of He I, Pa γ , and Pa δ , are not seen in the spectra of Gaia20bwa and Gaia20fgx. The visual extinctions and spectral types of the sources derived from the SEDs are similar to those of CTTS (e.g., Fiorellino et al. 2021) including EXors (Lorenzetti et al. 2009). We conclude, that the spectral properties of Gaia20bwa and Gaia20fgx, together with their accretion parameters, are more consistent with active CTTS, than with typical EXors.

5 SUMMARY

We have analyzed the light curves and optical and NIR spectra of two young stars which had *Gaia* alerts due to brightening episodes on a time-scale which is typical of the EXor class of young eruptive stars. The main results can be summarized as follows.

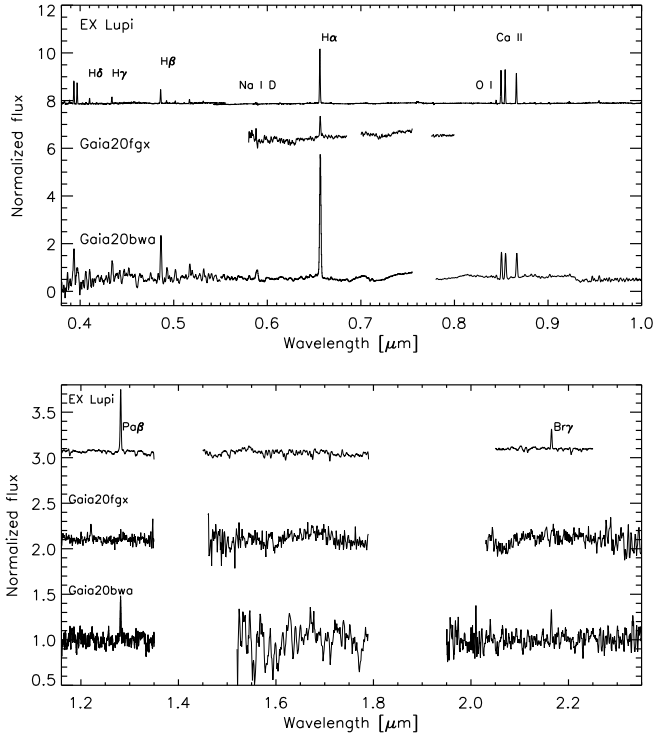


Figure 11. Comparison of the optical and NIR TNG spectra of Gaia20bwa and Gaia20fgx to those of EX Lupi, the proto-typical EXor during its latest outburst (Ábrahám et al., in prep.). The spectra of EX Lupi were smoothed to match their spectral resolution similar to that of the TNG spectra. For a better comparison, the optical fluxes of Gaia20bwa were multiplied by 0.6, the optical spectra of EX Lupi were multiplied by 0.4, and the NIR spectra of EX Lupi were multiplied by 2.

- The brightening episode of Gaia20bwa occurred on a time-scale of a year and few months with an amplitude of ~ 0.5 mag. Gaia20fgx showed two brightening episodes on a similar time-scale. Its second brightening episode which triggered the *Gaia* alerts system had an amplitude of ~ 2.5 mag.

- We have taken optical and NIR spectra of the sources using the TNG during their bright state, and NIR spectra for Gaia20fgx using the GTC during its fading. The hydrogen Balmer lines from $H\alpha$ to $H\delta$, $Pa\beta$, $Br\gamma$, and lines of Ca II, O I, and Na I were detected in emission in the spectra of Gaia20bwa. The $H\alpha$ and $Br\gamma$ lines were detected toward Gaia20fgx in emission in its bright state, with additional 2-0 and 3-1 bandhead features of CO in absorption and the $Pa\beta$ line showing an inverse P Cygni profile during its fading.

- Based on the $Br\gamma$ lines the accretion rate was found to be $(2.4 - 3.1) \times 10^{-8} M_{\odot} \text{ yr}^{-1}$ for Gaia20bwa and $(4.5 - 6.6) \times 10^{-8} M_{\odot} \text{ yr}^{-1}$ for Gaia20fgx during their bright state. The accretion rate of Gaia20fgx dropped by about a factor of 10, to $(6.01 - 7.0) \times 10^{-9} M_{\odot} \text{ yr}^{-1}$, on a time-scale of half a year.

- The accretion luminosities and rates measured for both sources are closer to those found for CTTS for similar stellar luminosities and masses than to those measured for young eruptive stars. However, the amplitude and time-scale of these brightening events place these two stars to a region of the parameter space, which is rarely populated by accreting young stellar objects. This suggests a new class of young stellar objects, which produce outbursts on a time-scale similar to young eruptive stars, but with smaller amplitudes,

possibly representing an intermediate case between variable CTTS and young eruptive stars.

ACKNOWLEDGEMENTS

We thank the referee for comments, which helped to improve our paper. This project has received funding from the European Research Council (ERC) under the European Union’s Horizon 2020 research and innovation programme under grant agreement No 716155 (SAC-CRED). We acknowledge support from the ESA PRODEX contract nr. 4000132054.

GM acknowledges funding from the European Union’s Horizon 2020 research and innovation programme under grant agreement No 101004141.

PZ and LW acknowledges the support from European Commission’s H2020 OPTICON grant No. 730890, OPTICON RadioNet Pilot grant No. 101004719 as well as Polish NCN grant Daina No. 2017/27/L/ST9/03221.

AP acknowledges support from Grant K-138962 of the National Research, Development and Innovation Office (NKFIH, Hungary).

LK acknowledges the financial support of the Hungarian National Research, Development and Innovation Office grant NKFIH PD-134784 and K-131508. LK is a Bolyai János Research Fellow.

Based on observations made with the Italian Telescopio Nazionale Galileo (TNG) operated by the Fundación Galileo Galilei (FGG) of the Istituto Nazionale di Astrofisica (INAF) at the Observatorio del Roque de los Muchachos (La Palma, Canary Islands, Spain).

SA, TG and BN received financial support from the project PRIN-INAF 2019 “Spectroscopically Tracing the Disk Dispersal Evolution” and by the project PRIN-INAF-MAIN-STREAM 2017 “Protoplanetary disks seen through the eyes of new-generation instruments”.

We acknowledge Ennio Poretti and Avet Harutyunyan for their help as TNG experts.

The Liverpool Telescope is operated on the island of La Palma by Liverpool John Moores University in the Spanish Observatorio del Roque de los Muchachos of the Instituto de Astrofísica de Canarias with financial support from the UK Science and Technology Facilities Council.

Based on observations made with the Gran Telescopio Canarias (GTC), installed in the Spanish Observatorio del Roque de los Muchachos of the Instituto de Astrofísica de Canarias, in the island of La Palma.

This work is (partly) based on data obtained with the instrument EMIR, built by a Consortium led by the Instituto de Astrofísica de Canarias. EMIR was funded by GRANTECAN and the National Plan of Astronomy and Astrophysics of the Spanish Government.

DATA AVAILABILITY

The data underlying this article will be shared on reasonable request to the corresponding author.

REFERENCES

- Ábrahám P., et al., 2009, *Nature*, **459**, 224
- Alcalá J. M., et al., 2017, *A&A*, **600**, A20
- Alcalá J. M., Manara C. F., France K., Schneider C. P., Arulanantham N., Miotello A., Günther H. M., Brown A., 2019, *A&A*, **629**, A108
- Allen T. S., et al., 2012, *ApJ*, **750**, 125

- Audard M., et al., 2014, in Beuther H., Klessen R. S., Dullemond C. P., Henning T., eds, *Protostars and Planets VI*. p. 387 ([arXiv:1401.3368](#)), [doi:10.2458/azu_uapress_9780816531240-ch017](#)
- Baffa C., et al., 2001, *A&A*, **378**, 722
- Bailer-Jones C. A. L., Rybizki J., Founesneau M., Demleitner M., Andrae R., 2021, *AJ*, **161**, 147
- Balcells M., et al., 2000, in Iye M., Moorwood A. F., eds, *Society of Photo-Optical Instrumentation Engineers (SPIE) Conference Series Vol. 4008*, *Optical and IR Telescope Instrumentation and Detectors*. pp 797–805, [doi:10.1117/12.395538](#)
- Bessell M. S., Brett J. M., 1988, *PASP*, **100**, 1134
- Blinova A. A., Romanova M. M., Lovelace R. V. E., 2016, *MNRAS*, **459**, 2354
- Bouvier J., et al., 1999, *A&A*, **349**, 619
- Bouvier J., et al., 2003, *A&A*, **409**, 169
- Briceño C., et al., 2019, *AJ*, **157**, 85
- Cardelli J. A., Clayton G. C., Mathis J. S., 1989, *ApJ*, **345**, 245
- Carpenter J. M., Hillenbrand L. A., Skrutskie M. F., 2001, *AJ*, **121**, 3160
- Chen X., Wang S., Deng L., de Grijs R., Yang M., Tian H., 2020, *ApJS*, **249**, 18
- Contreras Peña C., et al., 2017, *MNRAS*, **465**, 3011
- Cox A. W., Grady C. A., Hammel H. B., Hornbeck J., Russell R. W., Sitko M. L., Woodgate B. E., 2013, *ApJ*, **762**, 40
- Cruz-Sáenz de Miera F., et al., 2022, *ApJ*, **927**, 125
- Cutri R. M., et al., 2003, *2MASS All Sky Catalog of point sources.. NASA/IPAC Infrared Science Archive*
- Da Rio N., et al., 2016, *ApJ*, **818**, 59
- Fiorellino E., et al., 2021, *A&A*, **650**, A43
- Getman K. V., Feigelson E. D., Luhman K. L., Sicilia-Aguilar A., Wang J., Garmire G. P., 2009, *ApJ*, **699**, 1454
- Giannini T., et al., 2017, *ApJ*, **839**, 112
- Grankin K. N., Melnikov S. Y., Bouvier J., Herbst W., Shevchenko V. S., 2007, *A&A*, **461**, 183
- Gullbring E., Barwig H., Chen P. S., Gahm G. F., Bao M. X., 1996, *A&A*, **307**, 791
- Hartmann L., Calvet N., Gullbring E., D'Alessio P., 1998, *ApJ*, **495**, 385
- Henden A. A., Levine S., Terrell D., Welch D. L., 2015, in *American Astronomical Society Meeting Abstracts #225*. p. 336.16
- Herbig G. H., 1989, in *European Southern Observatory Conference and Workshop Proceedings*. pp 233–246
- Herbig G. H., 2008, *AJ*, **135**, 637
- Hillenbrand L. A., Findeisen K. P., 2015, *ApJ*, **808**, 68
- Hillenbrand L. A., et al., 2018, *ApJ*, **869**, 146
- Hillenbrand L. A., Reipurth B., Connelley M., Cutri R. M., Isaacson H., 2019, *AJ*, **158**, 240
- Hodapp K. W., et al., 2019, *AJ*, **158**, 241
- Hodapp K. W., et al., 2020, *AJ*, **160**, 164
- Hodgkin S. T., et al., 2021, *A&A*, **652**, A76
- Jayasinghe T., et al., 2019, *MNRAS*, **485**, 961
- Jordi C., Trullols E., Galadí-Enríquez D., 1996, *A&A*, **312**, 499
- Kanodia S., Wright J., 2018, *Research Notes of the American Astronomical Society*, **2**, 4
- Kóspál Á., Fiorellino E., Ábrahám P., Giannini T., Nisini B., 2022, *Research Notes of the American Astronomical Society*, **6**, 52
- Lorenzetti D., Larionov V. M., Giannini T., Arkharov A. A., Antonucci S., Nisini B., Di Paola A., 2009, *ApJ*, **693**, 1056
- Mamajek E. E., et al., 2015, *arXiv e-prints*, [p. arXiv:1510.06262](#)
- Manara C. F., Mordasini C., Testi L., Williams J. P., Miotello A., Lodato G., Emsenhuber A., 2019, *A&A*, **631**, L2
- Marton G., et al., 2019, *MNRAS*, **487**, 2522
- Masci F. J., et al., 2019, *PASP*, **131**, 018003
- Megeath S. T., et al., 2012, *AJ*, **144**, 192
- Meyer M. R., Calvet N., Hillenbrand L. A., 1997, *AJ*, **114**, 288
- Muzerolle J., Calvet N., Hartmann L., D'Alessio P., 2003, *ApJ*, **597**, L149
- Nagy Z., et al., 2021, *MNRAS*, **504**, 185
- Pascual S., Gallego J., Cardiel N., Eliche-Moral M. C., 2010, in *Mizumoto Y., Morita K. I., Ohishi M., eds, Astronomical Society of the Pacific Conference Series Vol. 434, Astronomical Data Analysis Software and Systems XIX*. p. 353
- Pecaut M. J., Mamajek E. E., 2013, *ApJS*, **208**, 9
- Piasecik A. S., Steele I. A., Bates S. D., Mottram C. J., Smith R. J., Barnsley R. M., Bolton B., 2014, in *Ramsay S. K., McLean I. S., Takami H., eds, Society of Photo-Optical Instrumentation Engineers (SPIE) Conference Series Vol. 9147, Ground-based and Airborne Instrumentation for Astronomy V*. p. 91478H, [doi:10.1117/12.2055117](#)
- Prato L., Simon M., Mazeh T., Zucker S., McLean I. S., 2002, *ApJ*, **579**, L99
- Scholz A., Xu X., Jayawardhana R., Wood K., Eisloffel J., Quinn C., 2009, *MNRAS*, **398**, 873
- Shappee B. J., et al., 2014, *ApJ*, **788**, 48
- Siess L., Dufour E., Forestini M., 2000, *A&A*, **358**, 593
- Siwak M., et al., 2018, *MNRAS*, **478**, 758
- Szegedi-Elek E., et al., 2020, *ApJ*, **899**, 130
- Tobin J. J., Hartmann L., Furesz G., Mateo M., Megeath S. T., 2009, *ApJ*, **697**, 1103

APPENDIX A: PHOTOMETRY

Table A1. Optical and near-infrared photometry of Gaia20bwa and Gaia20fgx. Uncertainties are typically 0.1 mag in the *B* filter, 0.05 mag in the *gVri* filters and 0.01 mag in the *JHK_s* filters.

Date	JD – 2 450 000	<i>B</i>	<i>g</i>	<i>V</i>	<i>r</i>	<i>i</i>	<i>J</i>	<i>H</i>	<i>K_s</i>	Telescope
Gaia20bwa										
2021-01-03	9218.36	...	17.607	...	16.701	15.507	Mt. Suhora
2021-01-22	9237.35	...	17.595	...	16.646	15.451	Mt. Suhora
2021-02-11	9257.41	12.930	12.164	11.741	TNG
2021-02-12	9258.31	18.147	...	17.315	16.712	15.580	RC80
2021-02-13	9259.29	18.004	...	17.073	16.596	15.456	RC80
2021-03-20	9294.30	17.462	...	16.865	16.458	15.454	RC80
2021-09-02	9459.58	15.869	RC80
2021-09-07	9464.60	19.291	...	18.218	17.496	15.805	RC80
2021-09-08	9465.58	17.974	17.414	15.694	RC80
2021-09-09	9466.57	18.267	17.521	15.823	RC80
2021-09-10	9467.58	19.249	...	18.069	17.376	15.741	RC80
2021-09-16	9473.63	18.117	17.824	15.914	RC80
2021-09-26	9483.53	19.068	...	18.052	17.406	15.774	RC80
2021-09-27	9484.57	18.120	17.718	15.872	RC80
2021-10-04	9491.53	18.257	17.540	15.861	RC80
2021-10-15	9502.63	19.298	...	18.199	17.471	15.713	RC80
2021-10-20	9507.59	18.296	17.564	15.815	RC80
2021-10-24	9512.49	18.191	17.403	15.749	RC80
2021-10-30	9517.60	19.484	...	18.295	17.495	15.811	RC80
2021-11-12	9530.59	19.498	...	18.182	17.504	15.806	RC80
2021-12-14	9562.56	19.371	...	18.219	17.499	15.821	RC80
2022-01-12	9592.39	18.232	17.557	15.843	RC80
2022-01-15	9595.33	15.809	RC80
2022-02-23	9634.26	19.397	...	18.263	17.517	15.834	RC80
Gaia20fgx										
2021-01-22	9237.28	...	19.629	...	17.523	16.306	Mt. Suhora
2021-01-27	9242.34	13.777	12.661	12.039	TNG
2021-02-13	9259.24	18.827	17.905	16.877	RC80
2021-02-14	9260.30	18.694	17.871	16.748	RC80
2021-05-05	9339.51	19.152	18.418	17.307	RC80
2021-05-09	9343.56	19.121	18.245	17.144	RC80
2021-06-19	9384.52	19.679	18.752	17.553	RC80
2021-07-06	9401.54	19.649	18.536	17.370	RC80
2021-07-09	9404.55	19.432	18.496	17.538	RC80
2021-07-12	9408.50	19.646	18.697	17.588	RC80
2021-07-24	9420.50	...	20.133	...	18.536	17.211	Mt. Suhora
2021-07-30	9425.51	19.204	18.585	17.688	RC80
2021-07-30	9426.45	19.750	18.736	17.676	RC80
2021-07-31	9427.45	19.641	18.671	17.634	RC80
2021-08-10	9437.45	19.089	18.119	17.049	RC80
2021-08-11	9438.49	19.212	18.169	16.986	RC80
2021-08-13	9439.50	19.257	18.272	17.062	RC80
2021-08-14	9440.54	19.462	18.523	17.329	RC80
2021-08-14	9441.45	19.128	18.226	17.197	RC80
2021-08-15	9441.52	...	20.421	...	18.526	17.248	Mt. Suhora
2021-08-18	9445.48	...	20.163	...	18.706	17.468	Mt. Suhora
2021-08-21	9447.53	19.535	18.444	17.238	RC80
2021-08-28	9454.60	19.457	18.538	17.329	RC80
2021-08-31	9457.61	20.143	18.682	17.382	RC80
2021-09-05	9463.42	18.098	17.164	RC80
2021-09-06	9464.41	19.142	18.227	17.083	RC80
2021-09-07	9465.37	19.039	18.152	16.981	RC80
2021-09-09	9466.51	18.876	18.058	16.975	RC80
2021-09-09	9467.47	19.595	18.555	17.318	RC80
2021-09-10	9468.38	19.055	18.279	17.228	RC80
2021-09-11	9469.36	19.664	18.613	17.505	RC80
2021-09-12	9470.44	19.463	18.579	17.403	RC80
2021-09-13	9471.34	19.514	18.555	17.354	RC80
2021-09-18	9476.43	14.060	12.856	12.229	GTC
2021-09-26	9483.50	19.326	18.280	17.012	RC80
2021-09-27	9484.59	19.252	18.151	16.867	RC80
2021-10-24	9511.58	19.560	18.514	17.481	RC80
2021-10-26	9513.58	18.303	17.643	RC80
2021-10-28	9515.57	19.926	18.914	17.812	RC80
2021-10-30	9517.56	18.893	17.920	RC80
2021-11-01	9519.58	18.376	17.564	RC80
2021-11-09	9527.56	19.579	18.900	17.752	RC80
2021-11-12	9530.52	19.744	19.177	18.137	RC80
2021-11-15	9533.55	19.092	18.390	RC80
2021-11-17	9535.52	20.236	19.281	18.249	RC80
2021-11-24	9542.54	19.031	18.034	RC80
2021-11-30	9548.52	18.954	18.139	RC80
2021-12-04	9552.51	19.016	18.424	RC80
2021-12-08	9556.51	18.972	18.126	RC80
2021-12-13	9562.40	19.748	18.940	17.930	RC80
2021-12-17	9566.45	18.882	18.055	RC80
2022-01-01	9581.44	19.262	18.355	17.175	RC80
2022-02-02	9613.69	19.019	18.382	17.433	RC80